

**Galvanic Replacement Synthesis of Multi-branched Gold Nanocrystals for Photothermal Cancer Therapy**

Journal:	<i>Journal of Materials Chemistry B</i>
Manuscript ID	TB-ART-03-2020-000748.R1
Article Type:	Paper
Date Submitted by the Author:	15-May-2020
Complete List of Authors:	Zhu, Dewei; University at Buffalo (SUNY), Chemical and Biological Engineering Liu, Yang; University at Buffalo - The State University of New York, Chemical and Biological Engineering Liu, Maixian; Shenzhen University, Optoelectrical Engineering Liu, Xin; Lawrence Berkeley National Laboratory, Prasad, Paras; Institute for Lasers, Photonics, and Biophotonics, Swihart, Mark T.; University at Buffalo (SUNY), Department of Chemical and Biological Engineering;

## ARTICLE

## Galvanic Replacement Synthesis of Multi-branched Gold Nanocrystals for Photothermal Cancer Therapy

Dewei Zhu<sup>a§</sup>, Yang Liu<sup>a§</sup>, Maixian Liu<sup>bc</sup>, Xin Liu<sup>a</sup>, Paras N. Prasad<sup>\*de</sup>, and Mark T. Swihart<sup>\*aef</sup>

Received 00th January 20xx,  
Accepted 00th January 20xx

DOI: 10.1039/x0xx00000x

We present a facile organic phase synthesis method for producing multi-branched gold nanocrystals (nanostars) with a broad localized surface plasmon resonance (LSPR) across near-infrared (NIR) to short-wave infrared (SWIR) wavelengths. In this approach, galvanic replacement of copper by gold, in seed particles produced in situ, initiates growth of multi-branched structures. The method enables broad tuning of the LSPR energy by manipulating the branch length, with peak LSPR absorbance tuned from 850 to 1880 nm, reaching SWIR wavelengths covering the second and third optical transparency windows in biological media, rarely achieved with noble metal plasmonic nanostructures. After a ligand-exchange process, the gold nanostars readily disperse in water while retaining their LSPR absorbance. The multi-branched Au NCs exhibit exceptionally high photothermal transduction efficiency, exceeding that of Au nanorods and nanoparticles, to which we make direct comparisons here. At the same time, their synthesis is much more straightforward than hollow structures like nanocages, nanoshells, and nanomatryoshkas that can also exhibit high photothermal efficiency at NIR wavelengths. In vitro photothermal heating of multi-branched Au nanocrystals in the presence of human cervical cancer cells causes effective cell ablation after 10 min laser irradiation. Cell viability assays demonstrate that the nanocrystals are biocompatible at doses required for photothermal therapy. These results suggest that the multi-branched Au NCs can serve as a new type of photothermal therapy agent and in other applications in which strong NIR to SWIR absorbers are needed.

### Introduction

The unique and useful optoelectronic and physicochemical properties of metal and semiconductor nanostructures have been shown to depend on many factors, including size, shape, and composition.<sup>1-4</sup> Controlling these parameters during synthesis allows the properties of nanocrystals to be precisely tuned for optimum performance in specific applications. Specifically, metal nanocrystals with anisotropic structures, including nanostars,<sup>5-6</sup> nanoflowers,<sup>7</sup> nanorods,<sup>8</sup> nanowires,<sup>9-11</sup> and nanoplates/sheets,<sup>12-13</sup> have each attracted specific

interest based upon their unique properties, including enhanced surface area, expression of high energy surface features, and ability to concentrate local electric fields, a desirable substrate feature in surface-enhanced Raman spectroscopy applications.<sup>14</sup>

Here, we report the synthesis of branched Au nanocrystals that consist predominantly of tripodal, tetrapodal and star-shaped decahedral structures, wherein the internal twin features of the nanocrystals break the symmetry of the face centered cubic (fcc) structure of the Au lattice and contribute to the emergence of branches. Significantly, Cu(I) was found to be a necessary reaction component for producing these branched structures, even though Cu was scarcely detectable in the final product. We thus propose that galvanic replacement occurs and contributes to the shaping of these nanocrystals by providing reactive locations at which gold has a higher deposition rate. In this way, galvanic replacement represents a new means of controlling growth kinetics and, thus, the final morphologies and properties adopted by nanocrystals. By extending the reaction time, longer branch length was achieved, accompanied by a red shift in LSPR. The peak of the LSPR absorbance was tuned by about a factor of two, from 850 nm to 1880 nm. This tuning is analogous to the red-shift with increasing aspect ratio that has been widely studied in Au NRs,<sup>15-16</sup> but extends to much longer wavelengths, well within the shortwave infrared (SWIR) wavelength range. Together, the nanostars of varying arm length provide strong absorbance over wavelengths from below 700 to beyond 2500 nm.

<sup>a</sup> Department of Chemical and Biological Engineering, University at Buffalo, The State University of New York, Buffalo, New York, 14260, USA.

<sup>b</sup> Key Laboratory of Optoelectronic Devices and Systems of Ministry of Education and Guangdong Province, College of Optoelectronic Engineering, Shenzhen University, Shenzhen, Guangdong, 518055, China.

<sup>c</sup> National-Regional Key Technology Engineering Laboratory for Medical Ultrasound, Guangdong Key Laboratory for Biomedical Measurements and Ultrasound Imaging, Department of Biomedical Engineering, School of Medicine, Shenzhen University, Shenzhen, 518055, China.

<sup>d</sup> Department of Chemistry, University at Buffalo, The State University of New York, Buffalo, New York, 14260, USA.

<sup>e</sup> Institute for Lasers, Photonics, and Biophotonics, University at Buffalo, The State University of New York, Buffalo, New York, 14260, USA.

<sup>f</sup> RENEW Institute, University at Buffalo, The State University of New York, Buffalo, New York, 14260, USA.

<sup>§</sup> Dewei Zhu and Yang Liu contributed equally to this work.

†Electronic Supplementary Information (ESI) available: [Details of photothermal transduction efficiency calculation; photograph of the system for photothermal heating experiments; TEM images of NCs obtained without Cu(I) and at different reaction times; photographs of NCs dispersion obtained at different reaction times; TEM image and photograph of Au nanostars after ligand exchange, TEM images of Au NPs and Au nanorods]. See DOI: 10.1039/x0xx00000x

Interest in nanoparticle-based strategies for combating cancer has grown rapidly over the past decade.<sup>17-18</sup> Compared with surgery, radiation therapy, chemotherapy, and other conventional approaches, nanoparticle treatments could be better targeted and less invasive, selectively killing tumor cells without damaging surrounding healthy tissue. Photothermal therapy (PTT), which employs heating of nanoparticles using near-infrared (NIR) light to ablate cancer cells, has attracted substantial research and clinical interest over the past few years.<sup>19-20</sup> Nanoparticles used for PTT should ideally be easily modified with surface ligands that serve to target specific cells or tissues *via* cell surface receptors. Most importantly, the optical absorbance of the nanoparticles should be as high as possible at near-IR wavelengths for which absorbance and scattering by biological media are minimized.<sup>21-22</sup>

Gold has been studied widely for its strong localized surface plasmon resonance (LSPR) absorbance. By manipulating their shape and size, the absorbance peak of gold nanoparticles can be tuned to NIR wavelengths. Anisotropic gold nanostructures, like nanorods,<sup>15-16</sup> nanoshells,<sup>23</sup> nanocages,<sup>24-25</sup> and nanostars<sup>26-27</sup> show high optical extinction coefficients in the NIR region and generate considerable heat under photoexcitation. Other nanomaterials developed for PTT, including carbon-based nanostructures,<sup>28-31</sup> organic compounds,<sup>32</sup> and other metal-based nanoparticles,<sup>33-34</sup> each have limitations such as low photothermal transduction efficiency, inadequate biocompatibility, or unfavorable absorbance spectra.

In this study, we report the synthesis and application of an anisotropic nanomaterial, multi-branched Au NCs, for possible use in photothermal cancer therapy based on its broad LSPR absorbance. *In vitro* studies show that the nanocrystals are effective photothermal transduction materials, exhibiting higher photothermal transduction efficiency than either gold nanorods (75×20 nm) or nanoparticles (~10 nm) when illuminated by a 980 nm laser beam under identical conditions.

## Experimental Section

**Chemicals.** Gold (III) chloride trihydrate (HAuCl<sub>4</sub>·3H<sub>2</sub>O, ≥99.99%), copper (I) chloride (99.995%), oleylamine (technical grade 70%), hexadecyltrimethylammonium bromide (CTAB, >98%), L-ascorbic acid (99+%), and sodium borohydride (NaBH<sub>4</sub>, 98.0%) were all purchased from Sigma Aldrich and used without further purification. Silver nitrate (AgNO<sub>3</sub>, 99+% metal basis) was purchased from Alfa Aesar. mPEG-thiol (mw. 2000) was purchased from Laysan Bio., Inc.

**Preparation of Multi-Branched Gold Nanostructures.** In a typical synthesis of the multi-branched gold nanostructures, 0.1 mmol CuCl(I) powder was mixed with 5 mL OAm and heated under a nitrogen atmosphere at 100°C for 30 min. The solution was then heated to 205 °C with mild stirring and held at this temperature to produce a transparent yellow solution, indicating the formation of organo-copper precursor in OAm. Then the solution was allowed to cool to 80 °C and a mixture of 0.15 mmol HAuCl<sub>4</sub>·3H<sub>2</sub>O, 1 mL OAm and 4 mL toluene was injected quickly. The solution turned blue immediately and

magnetic stirring was stopped after 2 min. The system was kept at 65°C for 45 min to produce fully-grown multi-branched nanostructures. The multi-branched Au NCs were separated by centrifugation and were dispersed in toluene. The separation-dispersion process was repeated. Finally, the NCs were dispersed in 3 mL chloroform as a stock solution for further use and characterization. Control experiments, without the copper precursor, were conducted in the same way. This led to the formation of ultrathin Au nanowires and Au nanoparticles, rather than nanostars.

**Preparation of 75×20 nm Gold Nanorods.** The method to obtain 75×20 nm Au NRs in this work was modified from previous reports.<sup>16, 35</sup> Briefly, 200 μL of 25 mM HAuCl<sub>4</sub>·3H<sub>2</sub>O aqueous solution was added into 10 mL of 0.1 M CTAB aqueous solution. The solution was stirred as 1 mL of ice-cold 0.01 M NaBH<sub>4</sub> was quickly added, followed by vigorous stirring for an additional 2 min. The color of the solution turned to light brown, indicating the formation of gold seeds with average size of ~3 nm. The seed solution was then kept in a water bath at 33 °C for further use. Meanwhile, to synthesize Au NRs, the same mixed solution of HAuCl<sub>4</sub>·3H<sub>2</sub>O and CTAB was prepared in a separate vial, with hydrochloric acid (0.16 M) and a small amount of Ag<sup>+</sup> ions (6 × 10<sup>-5</sup> M). 150 μL of 0.1 M ascorbic acid, a mild reducing agent, was added at room temperature to form a colorless growth solution. Finally, the growth solution was heated to 33 °C in a water bath and 12 μL of seed solution was gently injected into it. The formation of Au NRs proceeded without stirring at 33 °C for at least 3 hrs. Afterward, the bilayer CTAB-coated Au NRs were collected by centrifugation at 6600 g for 15 min and redispersed in HPLC water. The separation-dispersion process was repeated twice to remove the excess CTAB and unreacted precursor.

**Preparation of Aqueous Au Nanostars, Au NPs and Au NRs by Ligand Exchange.** For ligand exchange, 200 μL multi-branched Au NC stock solution was mixed with 50 mg mPEG-thiol (mw. 2000) and 2 mL chloroform under vigorous stirring for 2 hrs. The chloroform was evaporated using a rotary evaporator. The black film of PEG-terminated multi-branched Au NCs was firmly coated on the inner surface of the vial. The film was washed with hexane to remove the organic ligands that were substituted by PEG-SH through ligand exchange. The hexane wash solution remained clear, suggesting that it did not remove any multi-branched Au NCs. After complete removal of hexane, 2 mL HPLC water was added to disperse the PEG-terminated multi-branched Au NCs. The same procedure was applied to prepare aqueous dispersions of PEG-terminated Au NPs and Au NRs.

**Photothermal Heating Experiments.** The photothermal heating characteristics of all materials were measured with an infrared camera (FLIR Systems Inc., Boston, MA), using a 980 nm diode-laser (Q-Photonics) focused to 5/16 inch diameter with a biconvex lens as the excitation source, as shown in Fig. S2<sup>†</sup> in the Electronic Supplementary Material (ESM). All materials were dispersed in HPLC water and sonicated for 1 min. Then 1 mL of the sample under study was transferred to a 10 mm quartz cuvette. HPLC water was used as the control. The laser power was calibrated to a fluence of 1.34 W/cm<sup>2</sup> using a power

meter (Coherent Inc., Santa Clara, CA). Measurements were performed by irradiating the cuvette horizontally for 10 min and simultaneously collecting thermal images from above (i.e. not through a cuvette wall) using the infrared camera and ThermoVision software (FLIR Sys., Boston, MA).

**Cytotoxicity and In vitro Studies.** The MTT cell viability assay measures the absorbance of formazan produced by reduction of a tetrazolium compound by the mitochondria of viable cells. The absorbance is directly proportional to the number of live cells. For the *in vitro* cytotoxicity study, human cervical carcinoma cells (HeLa cells) growing in log phase were seeded into a 96-well cell culture plate at 10,000/well in Dulbecco's modified Eagle's medium (DMEM), which contains 10% fetal bovine serum, 4 mM glutamine, 100 U/mL penicillin, 100 mg/mL streptomycin, and 1% HEPES (hydroxyethylpiperazine ethane sulfonic acid). Cells were incubated at 37 °C under 5% CO<sub>2</sub> for 12 hrs. The cells were washed with DMEM and then incubated in the presence of PEGylated multi-branched Au NCs at different concentrations (50, 100 and 200 µg/mL, diluted in DMEM) for 24, 48 and 72 hours at 37 °C under 5% CO<sub>2</sub>. Subsequently, 20 µL of MTT (5 mg/mL) was added to each well of the 96-well assay plate and the cells were incubated for 2 more hours at 37 °C under 5% CO<sub>2</sub>. Afterward, the absorbance of the sample at 490 nm was recorded using a multiwell plate reader (Opsys MR, Dynex). Each experiment was repeated four times and untreated cells served as the control.

**In vitro Dark-Field Imaging.** Dark-field imaging was performed on a Nikon TE2000-U inverted microscope, equipped with a high numerical aperture dark-field condenser (Nikon, N.A. 1.20-1.43 oil immersion) and 100×/(0.5-1.3) NA Iris objective (DIC). The condenser delivers a narrow beam of white light from a tungsten lamp and the high NA oil immersion objective collects only the scattered light from the samples. The iris of the objective can be adjusted to optimize the collection of transmitted light. Images were captured with a CCD camera mounted on the microscope. The day prior to treatment, cells (HeLa and macrophages) were seeded on a square glass coverslip in a 35 mm well of a 6-well plate at 40-50% confluence. The cells were maintained in DMEM medium with 10% fetal bovine serum (FBS) and treated with PEGylated Au nanostars at a concentration of 50 µg/mL. The samples were incubated at 37 °C under 5% CO<sub>2</sub> for 3 hrs before imaging.

**In vitro Photothermal Therapy.** For *in vitro* photo-thermal therapy experiments, the cells were cultured by the same method mentioned above. After culturing, the cells were washed with DMEM and then incubated in the presence of PEGylated multi-branched Au NCs at different concentrations (50, 100 and 200 µg/mL, diluted in DMEM) for 4 hrs at 37 °C under 5% CO<sub>2</sub>. Control cells were incubated in fresh nanoparticle-free medium. After incubation, the medium for all cells, with or without nanoparticles, was replaced by fresh supplement medium to remove all unbound nanoparticles and dead cells. The cells were exposed in the well-plate under the NIR diode laser (Q-Photonics) for 10 min at 1.34 W/cm<sup>2</sup>. The irradiation was performed on both the cells incubated with the nanoparticles as well as the control cells. The medium was replaced again to remove dead cells and 20 µL of MTT (5

mg/mL) was added to each well, followed by 2 h incubation at 37 °C under 5% CO<sub>2</sub>. Finally, the absorbance data at 490 nm was recorded using a multiwell plate reader (Opsys MR, Dynex). Each experiment was repeated four times.

**Characterization.** Transmission electron microscopy (TEM) images were obtained using a JEOL JEM-2010 at an accelerating voltage of 200 kV. TEM samples were prepared by dropping a small amount of dilute nanoparticle dispersion onto a carbon-coated copper grid and allowing the solvent to evaporate. Energy Dispersive X-ray Spectroscopy (EDS) elemental analysis was obtained using an Oxford Instruments X-Max 20 mm<sup>2</sup> energy dispersive X-ray spectrometer detector within a Zeiss Auriga scanning electron microscope (SEM). Optical absorbance spectra of all nanocrystal dispersions in this work were measured using a Shimadzu 3600 UV-visible-NIR scanning spectrophotometer. Inductively Coupled Plasma Optical Emission Spectrometry (ICP-OES), using a Thermo Scientific iCAP 6000 system, was used to determine the concentrations of NCs in HPLC water. Each sample was rotary-evaporated to remove the organic solvent and then dissolved in aqua-regia (HCl/HNO<sub>3</sub>, volumetric ratio 3:1) for ICP-OES analysis.

## Results and discussion

Nearly all prior methods of preparing anisotropic Au nanostructures, including multi-branched Au NCs, have been conducted in water.<sup>36-38</sup> Those previously reported methods typically required hours or even days to achieve multi-branched Au NCs with long arm-length (>100 nm). Here, we demonstrate a novel method to produce multi-branched Au NCs with tunable arm-length (50-200 nm) in organic media using an organo-gold precursor, prepared by solubilizing HAuCl<sub>4</sub> with oleylamine. Excess OAm was present during the reaction and served as both a structure-directing agent and reducing agent.<sup>9, 39-40</sup> Cu(I) was

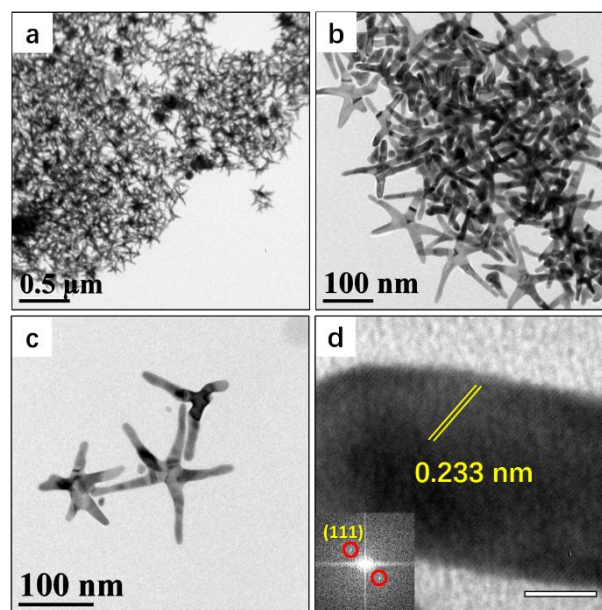
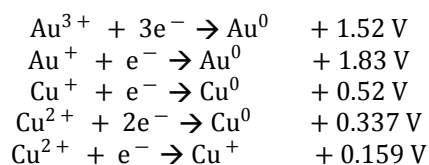


**Fig. 1** (a-c) TEM images of multi-branched Au NCs produced in the presence of Cu(I). HRTEM image (D) of the tip of one branch of the Au NCs, showing the lattice spacing of 2.33 Å corresponding to the (111) planes of gold. The inset shows the FFT of panel (d).

also solubilized with OAm and was present in a typical synthesis at a 3:2 molar ratio of Au-to-Cu. Although the TEM images of fully grown nanostars (Fig. 1a-c) do not suggest that any Au-Cu heterostructures have formed, the presence of Cu(I)-complex in the reaction medium was critical for the formation of multi-branched Au NCs. Under the same conditions, without adding the Cu precursor, the synthesis produced a mixture of ultrathin Au NWs and small Au NPs (Fig. S3<sup>†</sup>) With Cu(I) present, branched Au NCs were achieved in high yield with a variety of branching patterns.

To develop a reproducible protocol for preparing these interesting nanostructures, we experimentally explored the effects of reaction parameters and the mechanism controlling their formation. To explore the formation process of the nanostructures, samples were extracted by syringe from the same batch in a typical reaction at time points of 2, 10, 20, 30 and 40 min after injection of the gold precursor. TEM images of these samples (Fig. 2c-g) show the growth process of the branched Au NCs. Notably, the TEM and HRTEM images (Fig. 2a,b) of particles extracted after 2 min show the structure of the nuclei formed in the first stages of the reaction. The darker domains in Fig. 2a,b correspond to gold NCs that have nucleated on the surface of Cu-based NC cores. In contrast with the satellite domains with darker appearance and Au (111) lattice spacing, the core has a lattice spacing of 0.28 nm, which does not match any lattice spacing of cubic Au or Cu, but matches that of (110) planes of Au<sub>3</sub>Cu alloy.<sup>2,41</sup> Additional images of such heterogeneous nucleation products are provided in Fig S4<sup>†</sup>. We note that the lattice spacings of (110) planes of other Au-Cu alloys, i.e., AuCu and AuCu<sub>3</sub>, are 0.265 nm and 0.290 nm, respectively. Upon injection of gold precursors, the Au-Cu alloy seeds nucleated first, rather than metallic gold or copper nanocrystals. This is probably because formation energy (e.g., coherence energy and entropy of mixing) of Cu-Au alloy

nanocrystals is lower than monometallic Cu or Au.<sup>42-43</sup> The standard reduction potentials for these two metals (E vs. SHE) are:



Monometallic Cu should not be reduced prior to Au in the presence of both Au<sup>3+</sup>/Au<sup>+</sup>, Cu<sup>2+</sup>/Cu<sup>+</sup> precursors, while Au can replace Cu in existing Au<sub>3</sub>Cu lattice. The epitaxial growth of Au domains onto the Au<sub>3</sub>Cu core was also confirmed by FFT filter analysis. As shown in Figure S5, all satellite domains have the same set of FFT spots, which can be distinguished from those of the core domain with a lattice orientation mismatch of ~8°. All our observations together suggest that heterogeneous nucleation of gold occurred by epitaxial growth of the Au domains on Au<sub>3</sub>Cu templates. The formation of heterogeneous multi-pod NCs could be initiated by the galvanic replacement reaction:



The production of Cu(II) ions is consistent with the observation that the reaction media turned blue immediately upon injection of the gold precursor. Note that the nanoparticles collected and redispersed after 2 minutes reaction time form a yellow dispersion (Fig. S5 S6<sup>†</sup>), indicating that the blue colour of the reaction medium is from Cu<sup>2+</sup> ions, which remain in the supernatant after collection of nanoparticles by centrifugation. After the formation of the nuclei, the NCs continued growing to form polygonal multiply-twinned particles like those shown in Fig. 2c. With the extension of the reaction time to 20, 30 and 40 min, more and longer branches protruded from the polygonal

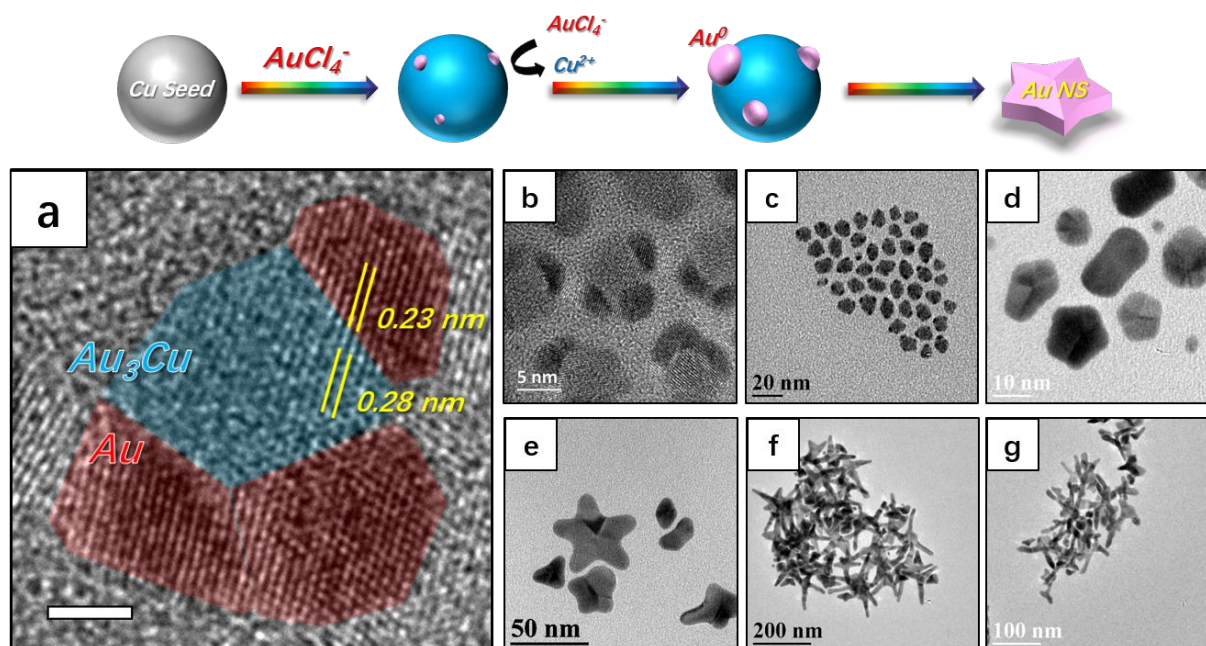


**Fig. 2** Top panel illustrates the nucleation and growth of Au nanostar. (a) Analysis of HRTEM image of nucleates from panel (a). The scale bar is 2 nm. (b-g) TEM images of NCs obtained at reaction time of (b,c) 2 min, (d) 10 min, (e) 20 min, (f) 30 min, (g) 40 min after injection of the Au precursor.

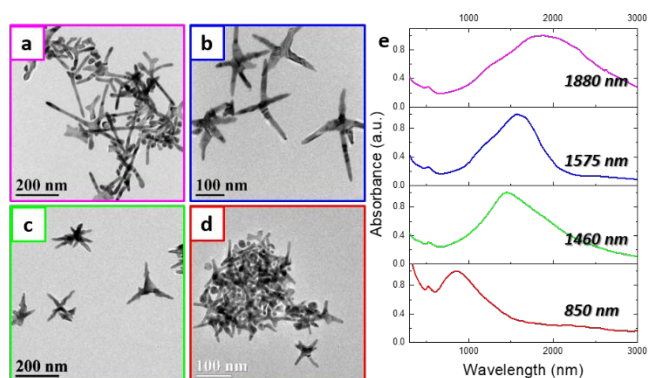


**Fig. 3** TEM images of multi-branched Au NCs with branch lengths of (a)  $\sim$ 200, (b)  $\sim$ 150, (c)  $\sim$ 100 and (d)  $\sim$ 50 nm. Optical absorbance (e) of the NCs with branch lengths of (a)  $\sim$ 200, (b)  $\sim$ 150, (c)  $\sim$ 100 and (d)  $\sim$ 50 nm.

nanocrystals (Fig. 2e-g). EDS and ICP-OES analysis (Table 1) showed the evolution from high copper content in the seed particles to negligible copper content in the final multi-branched structures.

**Table 1.** Results of EDS and ICP-OES elemental analysis of NCs obtained at different reaction time points.

Time Point (min)	Atomic (%)			
	EDS		ICP-OES	
	Cu	Au	Cu	Au
2	83.3	16.7	83.9	16.1
10	32.7	67.3	33.5	66.5
20	3.5	96.5	4.0	96.0
30	< 0.1	>99.9	< 0.1	>99.9
40	< 0.1	>99.9	< 0.1	>99.9

Typical branched Au NCs with optimized morphology and yield were produced when the NCs were grown at a relatively low temperature of 65 °C. Fig. S6 S7<sup>†</sup> shows TEM images of samples produced at temperatures of 90 °C, 120 °C and 150 °C. Synthesis at higher temperature produced more spherical and polygonal gold NCs. Nucleation at higher temperature leads to more nucleated NCs, and nucleation of both gold and copper NCs. As a result, the amount of remaining precursors relative to the number of nucleated NCs is lower, and the remaining precursor is insufficient to achieve fully grown branched structures with extended branches. As the reaction temperature was increased, the fraction of spherical NCs produced also increased.

As mentioned above, for synthesis at low temperature, the branches became longer with increased reaction time. This provides a method to produce multi-branched Au NCs with adjustable branch length, and therefore tunable LSPR energy and corresponding absorbance spectrum. As shown in Fig. 3, the branch length of the multi-branched NCs could be adjusted from  $\sim$ 50 nm to more than 200 nm. The LSPR absorbance spectra of the multi-branched NCs exhibit two peaks resulting from the transverse and longitudinal LSPR, similar to spectra of Au nanorods. The relatively weak LSPR peak located at around 520 nm is similar in each case, while the other peak in the NIR region is red-shifted with increasing branch length, across the NIR region from 850 nm to 1880 nm as shown in Fig. 3e.

Prior to examination of their photothermal conversion performance, the multi-branched Au NCs were first subjected to ligand exchange to transfer them into water. After the ligand exchange procedure, as described in the Experimental Section, we obtained a transparent light purple aqueous dispersion of the NCs as shown in Fig. S7 S8<sup>†</sup>. Easy ligand exchange is a beneficial feature of these Au NCs. For Au nanostructures synthesized in water with cationic surfactants like CTAB,<sup>16</sup> complete removal of the water-soluble and cytotoxic surfactants can be challenging. In contrast, the hydrophobic oleylamine ligands used here do not transfer into the aqueous phase after they are displaced by thiol-PEG. TEM imaging (Fig. S7 S8<sup>†</sup>) showed that the dispersity and morphology of multi-branched Au NCs were unchanged by their transfer into water. We measured the temperature elevation of pure HPLC water (control) and aqueous multi-branched Au NC dispersions of different concentrations under 980 nm laser illumination at an intensity of 1.34 W/cm<sup>2</sup>. Representative temperature change curves during the heating and cooling process are shown in Fig. 4a. The control experiment using pure water shows that the temperature only increased by 5.6 °C from room temperature (24 °C) after 10 min of laser irradiation. As the concentration of the multi-branched Au NCs increased from 50 to 200  $\mu$ g/mL (0.005 to 0.02 wt % or 50 to 200 ppm), the temperature of the NC dispersions increased by 16.8 to 23.1 °C, as shown in Fig. 4a. The temperature change ( $\Delta T$ ) was plotted versus the concentration of the multi-branched Au NCs in the aqueous dispersion (Fig. 4b). We note that the branched Au NCs did not undergo shape evolution after 980 nm laser irradiation (Figure S8c), indicating the stability of the materials under mild heating like that associated with PTT. At higher NC concentrations, the additional light absorbed upon increasing the concentration is

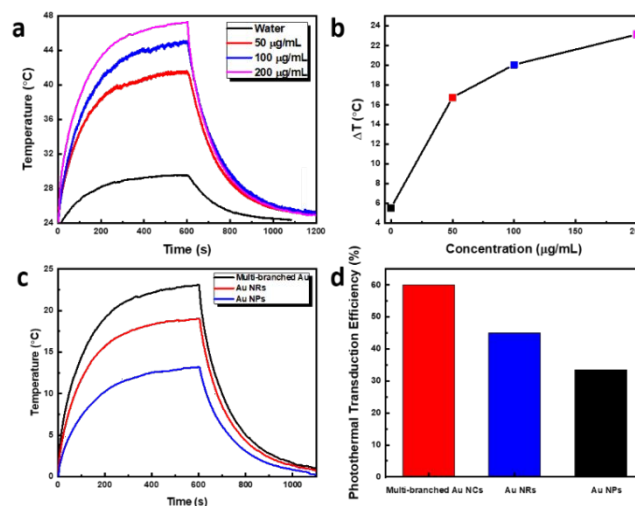


**Fig. 4** (a) The photothermal response of PEGylated multi-branched Au NCs dispersed in HPLC water at concentrations of 50, 100 and 200  $\mu$ g/mL. The laser heating of the water contributes approximately 5.6 °C to the overall change in temperature after 10 min (black). (b) Plot of temperature change ( $\Delta T$ ) over a period of 10 min versus the concentration of the multi-branched Au NC aqueous dispersion. (c) The photothermal response of PEGylated multi-branched Au NCs (red), Au nanorods (blue) and  $\sim$ 10 nm Au nanoparticles (black) dispersed in HPLC water at a concentration of 200  $\mu$ g/mL, obtained by irradiating 1 mL aliquots of each solution for 10 min with a 980 nm diode laser (5/16-inch spot size, fluence of 1.34 W/cm<sup>2</sup>). (d) Photothermal transduction efficiencies at 980 nm for the multi-branched Au nanocrystals, Au nanorods and  $\sim$ 10 nm Au nanoparticles.

smaller, and the heat loss to the surroundings is larger; thus, the temperature increase saturates with increasing concentration. Further increasing the concentration beyond 200  $\mu\text{g}/\text{mL}$  would not produce much further increase in temperature.

To calculate the photothermal transduction efficiency of the multi-branched Au NCs, we followed a widely used method modified from the approach developed by Roper et al.<sup>24, 44-45</sup> The aqueous dispersion of multi-branched Au NCs contained in a 1 cm quartz cuvette was exposed to a 980 nm continuous laser beam at a flux of 1.34  $\text{W}/\text{cm}^2$  for 10 min. After the laser was turned off, the temperature gradually decreased to room temperature. The temperature changes of NC dispersions at a fixed concentration of 200  $\mu\text{g}/\text{mL}$  were recorded by a thermal camera and plotted in Fig. 4c (black curve) as a function of time. The heat transfer rate from the cuvette to the surroundings was determined from the cooling curve, and this value was used to determine the total heat added to the cuvette during laser illumination. Combining that with the measured absorbance allowed determination of the photothermal transduction efficiency, as described in detail in the supporting information. Using this approach, the photothermal transduction efficiency of the multi-branched Au NCs was calculated to be 60% (red column in Fig. 4d). To compare the photothermal transduction efficiency of multi-branched Au NCs to other PTT agents, we prepared  $\sim 10$  nm gold nanoparticles and 75 $\times$ 20 nm gold nanorods. The morphology, size, and the absorbance spectra of these Au NCs are shown in Fig. S8 S9. These NCs were treated by the same procedures, ligand exchange and photothermal heating experiments. The absorbance spectra and photothermal heating-cooling data were measured in HPLC water at a concentration of 200  $\mu\text{g}$  NCs/mL (Fig. 4c, red and blue curves). According to the data obtained from Fig. 4c, the photothermal transduction efficiencies of gold nanorods ( $r = 10$  nm,  $L = 75$  nm) and nanospheres ( $r = 5$  nm) were determined to be 46% and 33%, respectively at 980 nm (Fig. 4d). As the measurement and analysis were conducted by identical means, the comparison of this transduction efficiency between samples is meaningful. Thus, we conclude that the transduction efficiency at 980 nm of multi-branched Au NCs is higher than that of both Au NRs and Au NPs at the same wavelength. Lack of standardization of photothermal transduction efficiency experiments makes comparisons of measurements made under different conditions difficult. However, some comparisons are possible. Cole et al.<sup>23</sup> found that Au/Au<sub>2</sub>S nanoshells had slightly lower transduction efficiency than Au NRs, while Au/SiO<sub>2</sub> nanoshells had much lower transduction efficiency (at 815 nm). Later, Ayala-Orozco et al.<sup>46</sup> showed that Au/SiO<sub>2</sub>/Au nanomatryoshkas had higher transduction efficiency than Au/SiO<sub>2</sub> nanoshells, similar to that of Au/Au<sub>2</sub>S nanoshells and Au NRs (at 810 nm). Wang et al.<sup>25</sup> compared Au NRs, Au nanocages, and Au nanohexapods and found very similar transduction efficiency for all three at the same optical density and illumination intensity (at 805 nm). Thus, based on the observed higher transduction efficiency compared to Au NRs, we expect the transduction efficiency of the Au nanostars presented here to be comparable to or better than complex structures such as nanomatryoshkas and nanoshells, with the

added benefit of being able to extend the operating wavelength further into the infrared, covering second and third optical transparency windows in biological media which allow reduced scattering of light in tissues.<sup>47</sup> The sum of the absorption and scattering is the extinction, and photothermal efficiency depends upon the fraction of extinction that is attributable to absorption. That is, the ratio between absorption and scattering cross-section  $Q_{\text{abs}}/Q_{\text{scat}}$  determines the efficiency.<sup>48</sup> Although relatively large nanostructures may have higher scattering to absorption ratios, we expect that the high local curvature, multi-tip structures, and potential lattice strains in gold nanostars can also influence the scattering to absorption ratio.<sup>49-51</sup> In addition, comparing nanostars to nanorods, more resonance modes are possible in the branched structures, and these can be excited in more orientations of the overall structure.

Before conducting an *in vitro* photothermal therapy experiment, we carried out a cytotoxicity test, without photothermal heating, to ensure that the multi-branched Au NCs were not toxic at the concentrations needed for PTT. The biocompatibility of the multi-branched Au NCs was tested using the MTT cell viability assay with human cervical carcinoma cells (HeLa cells). Cells were incubated in the presence of PEGylated multi-branched Au NCs at different concentrations (50, 100, or 200  $\mu\text{g}/\text{mL}$ , diluted in DMEM) for periods of 24, 48 and 72 hours at 37  $^{\circ}\text{C}$  under 5% CO<sub>2</sub>, and then the cell viability was assessed using the MTT assay. Each experiment was repeated four times and untreated cells served as the control. As shown in Fig. 5a, negligible cell death was observed for a concentration of 50  $\mu\text{g}/\text{mL}$  of the Au NCs. A concentration of 100  $\mu\text{g}/\text{mL}$  had no obvious effect on the HeLa cells within the first 48 hrs, but after 72 hrs, the sample incubated with multi-branched Au NCs at 100

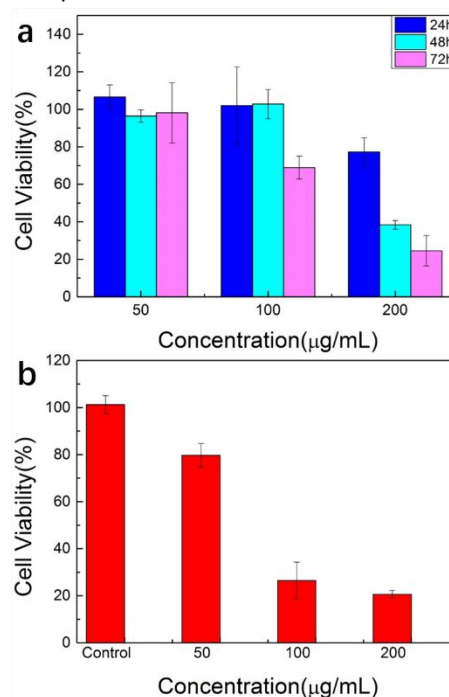


Fig. 5 Viability of HeLa cells incubated with different concentration of multi-branched Au NCs (A) without NIR irradiation, measured after 24, 48 and 72 hours and (B) with NIR irradiation (980 nm, 1.34  $\text{W}/\text{cm}^2$  for 10 min), within a few minutes of the end of irradiation.

$\mu\text{g/mL}$  showed  $\sim 30\%$  cell death. Significant loss of cell viability was also observed in the samples incubated with the highest NC concentration of  $200 \mu\text{g/mL}$ . The PEGylated NPs were then used for *in vitro* imaging using dark-field microscopy. As shown in Fig. S10, HeLa cells incubated with Au NCs at a concentration of  $50 \mu\text{g/mL}$  qualitatively demonstrate extensive nanoparticle uptake as evidenced by coloured bright spots within the cytoplasm of the cells. The PEGylated multi-branched Au NCs appear to accumulate in vesicles within macrophages and HeLa cells, suggesting an endocytotic uptake pathway that allows the cells to remain viable.<sup>1, 52</sup>

We next conducted *in vitro* photothermal therapy experiments by irradiating HeLa cells that had been incubated for 4 hrs in the presence of PEGylated multi-branched Au NCs at different concentrations ( $50$ ,  $100$  and  $200 \mu\text{g/mL}$ , diluted in DMEM) under the NIR diode laser ( $980 \text{ nm}$ ,  $10 \text{ min}$  at  $1.34 \text{ W/cm}^2$ ).<sup>53-56</sup> While this illumination intensity exceeds safe skin exposure levels established for occupational safety and health, it is lower than that used in many photothermal therapy demonstrations, including clinical trials of photothermal therapy using gold nanoshells.<sup>57</sup> Control cells were incubated in fresh nanoparticle-free medium and irradiated under the same conditions. The MTT cell viability test (Fig. 5b) showed that the photothermal heating generated by illumination of the multi-branched Au NCs could effectively ablate the HeLa cells. The lowest concentration ( $50 \mu\text{g/mL}$ ) produced a comparatively low rate of cell death, only  $\sim 20\%$  reduction in viable cells. However, for a concentration of  $100 \mu\text{g/mL}$  in the incubation stage, dramatic cell death ( $>70\%$ ) was observed after irradiation. Further increasing nanocrystal concentration beyond  $100 \mu\text{g/mL}$  did not produce much further decrease in the number of viable cells. Thus, for the specific incubation conditions and laser fluence used in this study, the critical concentration for inducing substantial cell death was between  $50$  and  $100 \mu\text{g/mL}$  of the Au NCs. Without illumination, incubation of cells with concentrations in this range, for up to 48 hours, had negligible effect on cell viability. Thus, the multi-branched Au NCs provide a significant range of conditions for which PTT is effective, but for which intrinsic toxicity of the Au NCs (without illumination) is negligible.

## Conclusions

We have presented a facile organic phase synthesis method for producing multi-branched gold nanocrystals (nanostars) with a broad localized surface plasmon resonance (LSPR) across near-infrared (NIR) wavelengths and into the short-wave infrared (SWIR) range, tunable by manipulating the branch length. This synthesis is based on *in situ* formation of copper nanoparticle seeds followed by galvanic exchange of Cu for Au that initiates branch growth. After a ligand-exchange process, the gold nanostars readily disperse in water while retaining their LSPR absorbance. Upon illumination with a  $980 \text{ nm}$  laser beam, the multi-branched Au NCs exhibited much higher photothermal transduction efficiency ( $60\%$ ) than Au nanorods ( $46\%$ ) or spherical Au nanoparticles ( $33\%$ ), for a fixed concentration of  $200 \mu\text{g/mL}$  and laser wavelength of  $980 \text{ nm}$ . *In vitro*

photothermal heating of multi-branched Au nanocrystals in the presence of human cervical cancer cells caused effective cell ablation after  $10 \text{ min}$  laser irradiation. Cell viability assays demonstrated that the nanocrystals are biocompatible at doses needed for photothermal therapy. These results suggest that the multi-branched Au NCs may serve as a new class of potential photothermal therapy agent.

## Conflicts of interest

There are no conflicts to declare

## Acknowledgements

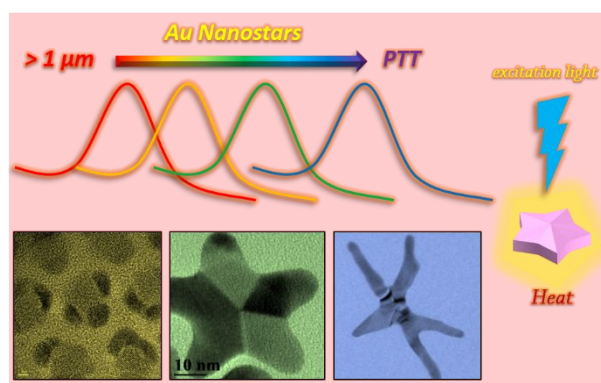
This work was supported, in part, by the New York State Center of Excellence in Materials Informatics and by the Air Force Office of Scientific Research (FA9550-11-1-0121).

## Notes and references

- Liu, X.; Lee, C.; Law, W. C.; Zhu, D.; Liu, M.; Jeon, M.; Kim, J.; Prasad, P. N.; Kim, C.; Swihart, M. T., *Nano Lett.* **2013**, *13* (9), 4333-4339.
- Wang, Z.; Ju, Y.; Tong, S.; Zhang, H.; Lin, J.; Wang, B.; Hou, Y., *Nanoscale Horiz.* **2018**, *3* (6), 624-631.
- Liu, Y.; Zhang, H.; Behara, P. K.; Wang, X.; Zhu, D.; Ding, S.; Ganesh, S. P.; Dupuis, M.; Wu, G.; Swihart, M. T., *ACS Appl. Mater. Interfaces* **2018**, *10* (49), 42417-42426.
- Liu, Y.; Zhu, D.; Hu, Y.; Swihart, M. T.; Wei, W., *Langmuir* **2018**, *34* (46), 13905-13909.
- Huang, L.; Zhang, W.; Li, P.; Song, Y.; Sheng, H.; Du, Y.; Wang, Y. G.; Wu, Y.; Hong, X.; Ding, Y.; Yuan, X.; Zhu, M., *Nano Res.* **2019**, *12* (5), 1147-1153.
- Tsoulos, T. V.; Atta, S.; Lagos, M. J.; Beetz, M.; Batson, P. E.; Tsilomelekis, G.; Fabris, L., *Nanoscale* **2019**, *11* (40), 18662-18671.
- Bai, S.; Gao, C.; Low, J.; Xiong, Y., *Nano Res.* **2019**, *12* (9), 2031-2054.
- Wang, N.; Zhao, Z.; Lv, Y.; Fan, H.; Bai, H.; Meng, H.; Long, Y.; Fu, T.; Zhang, X.; Tan, W., *Nano Res.* **2014**, *7* (9), 1291-1301.
- Zhu, W.; Zhang, Y. J.; Zhang, H.; Lv, H.; Li, Q.; Michalsky, R.; Peterson, A. A.; Sun, S., *J. Am. Chem. Soc.* **2014**, *136* (46), 16132-16135.
- Yang, Y.; Jin, H.; Kim, H. Y.; Yoon, J.; Park, J.; Baik, H.; Joo, S. H.; Lee, K., *Nanoscale* **2016**, *8* (33), 15167-15172.
- An, H.; Khi, N. T.; Yoon, J.; Lee, H.; Baik, H.; Sohn, J. H.; Lee, K., *Nanoscale* **2015**, *7* (18), 8309-8314.
- Luo, M.; Zhao, Z.; Zhang, Y.; Sun, Y.; Xing, Y.; Lv, F.; Yang, Y.; Zhang, X.; Hwang, S.; Qin, Y.; Ma, J. Y.; Lin, F.; Su, D.; Lu, G.; Guo, S., *Nature* **2019**, *574* (7776), 81-85.
- Chen, M.; Tang, S.; Guo, Z.; Wang, X.; Mo, S.; Huang, X.; Liu, G.; Zheng, N., *Adv. Mater.* **2014**, *26* (48), 8210-6.
- Nikoobakht, B.; Wang, J.; El-Sayed, M. A., *Chem. Phys. Lett.* **2002**, *366* (1), 17-23.
- Huang, X.; Neretina, S.; El-Sayed, M. A., *Adv. Mater.* **2009**, *21* (48), 4880-4910.
- Nikoobakht, B.; El-Sayed, M. A., *Chem. Mater.* **2003**, *15* (10), 1957-1962.
- Fan, W.; Yung, B.; Huang, P.; Chen, X., *Chem. Rev.* **2017**, *117* (22), 13566-13638.

18. Cheng, L.; Wang, C.; Feng, L.; Yang, K.; Liu, Z., *Chem. Rev.* **2014**, *114* (21), 10869-10939.
19. Zhu, D.; Liu, M.; Liu, X.; Liu, Y.; Prasad, P. N.; Swihart, M. T., *J. Mater. Chem. B* **2017**, *5* (25), 4934-4942.
20. Zhang, S.; Sun, C.; Zeng, J.; Sun, Q.; Wang, G.; Wang, Y.; Wu, Y.; Dou, S.; Gao, M.; Li, Z., *Adv. Mater.* **2016**, *28* (40), 8927-8936.
21. Hong, G.; Antaris, A. L.; Dai, H., *Nat. Biomed. Eng.* **2017**, *1* (1), 0010.
22. Ju, Y.; Zhang, H.; Yu, J.; Tong, S.; Tian, N.; Wang, Z.; Wang, X.; Su, X.; Chu, X.; Lin, J.; Ding, Y.; Li, G.; Sheng, F.; Hou, Y., *ACS Nano* **2017**, *11* (9), 9239-9248.
23. Cole, J. R.; Mirin, N. A.; Knight, M. W.; Goodrich, G. P.; Halas, N. J., *J. Phys. Chem. C* **2009**, *113* (28), 12090-12094.
24. Piao, J. G.; Gao, F.; Li, Y.; Yu, L.; Liu, D.; Tan, Z. B.; Xiong, Y.; Yang, L.; You, Y. Z., *Nano Res.* **2018**, *11* (6), 3193-3204.
25. Wang, Y.; Black, K. C.; Luehmann, H.; Li, W.; Zhang, Y.; Cai, X.; Wan, D.; Liu, S. Y.; Li, M.; Kim, P.; Li, Z. Y.; Wang, L. V.; Liu, Y.; Xia, Y., *ACS Nano* **2013**, *7* (3), 2068-2077.
26. Jauffred, L.; Samadi, A.; Klingberg, H.; Bendix, P. M.; Oddershede, L. B., *Chem. Rev.* **2019**, *119* (13), 8087-8130.
27. Vines, J. B.; Yoon, J. H.; Ryu, N. E.; Lim, D. J.; Park, H., *Front. Chem.* **2019**, *7* (167), 167.
28. Moon, H. K.; Lee, S. H.; Choi, H. C., *ACS Nano* **2009**, *3* (11), 3707-13.
29. Fisher, J. W.; Sarkar, S.; Buchanan, C. F.; Szot, C. S.; Whitney, J.; Hatcher, H. C.; Torti, S. V.; Rylander, C. G.; Rylander, M. N., *Cancer Res.* **2010**, *70* (23), 9855-64.
30. Yang, K.; Zhang, S.; Zhang, G.; Sun, X.; Lee, S. T.; Liu, Z., *Nano Lett.* **2010**, *10* (9), 3318-23.
31. Robinson, J. T.; Tabakman, S. M.; Liang, Y.; Wang, H.; Casalongue, H. S.; Vinh, D.; Dai, H., *J Am Chem Soc* **2011**, *133* (17), 6825-31.
32. Yang, J.; Choi, J.; Bang, D.; Kim, E.; Lim, E. K.; Park, H.; Suh, J. S.; Lee, K.; Yoo, K. H.; Kim, E. K.; Huh, Y. M.; Haam, S., *Angew. Chem. Int. Ed. Engl.* **2011**, *50* (2), 441-444.
33. Huang, X.; Tang, S.; Mu, X.; Dai, Y.; Chen, G.; Zhou, Z.; Ruan, F.; Yang, Z.; Zheng, N., *Nat. Nanotechnol.* **2011**, *6* (1), 28-32.
34. Wang, S.; Chen, K. J.; Wu, T. H.; Wang, H.; Lin, W. Y.; Ohashi, M.; Chiou, P. Y.; Tseng, H. R., *Angew. Chem. Int. Ed. Engl.* **2010**, *49* (22), 3777-3781.
35. Liu, M.; Law, W. C.; Kopwiththaya, A.; Liu, X.; Swihart, M. T.; Prasad, P. N., *Chem Commun (Camb)* **2013**, *49* (81), 9350-9352.
36. Hao, E.; Bailey, R. C.; Schatz, G. C.; Hupp, J. T.; Li, S., *Nano Lett.* **2004**, *4* (2), 327-330.
37. Liu, H.; Xu, Y.; Qin, Y.; Sanderson, W.; Crowley, D.; Turner, C. H.; Bao, Y., *J. Phys. Chem. C* **2013**, *117* (33), 17143-17150.
38. Webb, J. A.; Erwin, W. R.; Zarick, H. F.; Aufrecht, J.; Manning, H. W.; Lang, M. J.; Pint, C. L.; Bardhan, R., *J. Phys. Chem. C* **2014**, *118* (7), 3696-3707.
39. Mourdikoudis, S.; Liz-Marzan, L. M., *Chem. Mater.* **2013**, *25* (9), 1465-1476.
40. Lu, X.; Tuan, H. Y.; Korgel, B. A.; Xia, Y., *Chemistry-A European Journal* **2008**, *14* (5), 1584-1591.
41. Mendoza-Cruz, R.; Bazán-Díaz, L.; Velázquez-Salazar, J. J.; Samaniego-Benitez, J. E.; Ascencio-Aguirre, F. M.; Herrera-Becerra, R.; José-Yacamán, M.; Guisbiers, G., *Nanoscale* **2017**, *9* (27), 9267-9274.
42. He, R.; Wang, Y. C.; Wang, X.; Wang, Z.; Liu, G.; Zhou, W.; Wen, L.; Li, Q.; Wang, X.; Chen, X.; Zeng, J.; Hou, J. G., *Nat. Commun.* **2014**, *5* (1), 4327.
43. Yin, J.; Shan, S. Y.; Yang, L. F.; Mott, D.; Malis, O.; Petkov, V.; Cai, F.; Ng, M. S.; Luo, J.; Chen, B. H.; Engelhard, M.; Zhong, C. J., *Chem. Mater.* **2012**, *24* (24), 4662-4674.
44. Tian, Q.; Jiang, F.; Zou, R.; Liu, Q.; Chen, Z.; Zhu, M.; Yang, S.; Wang, J.; Wang, J.; Hu, J., *ACS Nano* **2011**, *5* (12), 9761-9771.
45. Roper, D. K.; Ahn, W.; Hoepfner, M., *J. Phys. Chem. C* **2007**, *111* (9), 3636-3641.
46. Ayala-Orozco, C.; Urban, C.; Knight, M. W.; Urban, A. S.; Neumann, O.; Bishnoi, S. W.; Mukherjee, S.; Goodman, A. M.; Charron, H.; Mitchell, T.; Shea, M.; Roy, R.; Nanda, S.; Schiff, R.; Halas, N. J.; Joshi, A., *ACS Nano* **2014**, *8* (6), 6372-6381.
47. Smith, A. M.; Mancini, M. C.; Nie, S., *Nat. Nanotechnol.* **2009**, *4* (11), 710-711.
48. Bi, C.; Chen, J.; Chen, Y.; Song, Y.; Li, A.; Li, S.; Mao, Z.; Gao, C.; Wang, D.; Möhwald, H.; Xia, H., *Chem. Mater.* **2018**, *30* (8), 2709-2718.
49. Chen, H.; Shao, L.; Ming, T.; Sun, Z.; Zhao, C.; Yang, B.; Wang, J., *Small* **2010**, *6* (20), 2272-2280.
50. Jiang, K.; Smith, D. A.; Pinchuk, A., *J. Phys. Chem. C* **2013**, *117* (51), 27073-27080.
51. Qin, Z.; Wang, Y.; Randrianalisoa, J.; Raeesi, V.; Chan, W. C.; Lipinski, W.; Bischof, J. C., *Sci. Rep.* **2016**, *6* (1), 29836.
52. Potara, M.; Nagy-Simon, T.; Craciun, A. M.; Suarasan, S.; Licarete, E.; Imre-Lucaci, F.; Astilean, S., *ACS Appl. Mater. Interfaces* **2017**, *9* (38), 32565-32576.
53. Daou, T. J.; Li, L.; Reiss, P.; Jossierand, V.; Texier, I., *Langmuir* **2009**, *25* (5), 3040-3044.
54. Li, A.; Luehmann, H. P.; Sun, G.; Samarajeewa, S.; Zou, J.; Zhang, S.; Zhang, F.; Welch, M. J.; Liu, Y.; Wooley, K. L., *ACS Nano* **2012**, *6* (10), 8970-82.
55. Wang, W.; Kong, Y.; Jiang, J.; Tian, X.; Li, S.; Akshath, U. S.; Tiede, C.; Hondow, N.; Yu, A.; Guo, Y.; Zhou, D., *Nanoscale* **2020**.
56. Liu, K.; Liu, K.; Liu, J.; Ren, Q.; Zhao, Z.; Wu, X.; Li, D.; Yuan, F.; Ye, K.; Li, B., *Nanoscale* **2020**, *12* (5), 2902-2913.
57. Nanospectra Biosciences, I., Pilot Study of AuroLase™ <http://clinicaltrials.gov/show/NCT00848042> **2008**.

## Table of Content Graphics



We synthesized multi-branched gold nanostars with broad localized surface plasmon resonance absorbance across near-infrared to short-wave infrared wavelengths. In vitro photothermal heating of Au nanostars in the presence of human cervical cancer cells led to effective cell ablation after 10 min laser irradiation.